BIMETALS

Materials used in industry are often required to satisfy a set of properties (mechanical/thermal, electrical, magnetic, mechanical/environmental) that are difficult for a single material to meet. Sometimes it is possible to select a material with a suitable combination of properties, but as the severity of the requirements increases, the availability of suitable materials becomes very limited. A rational way of resolving such problems is to design the component so that it properly combines the properties of two different materials. This requirement has resulted in the development of bimetals.

As an example, for components demanding both high strength and corrosion resistance, the surface (e.g., stainless steel, Ni alloy, Ti) can be designed to resist attack by the environment and the bulk (e.g., carbon steel) can be optimized for load-bearing. In other applications, corrosion resistance and electric conductivity are required, and copper clad with Ti, Ni alloys or stainless steel bimetals have been developed. When mechanical strength is required instead of corrosion resistance, carbon steel and copper are used. In other cases, through an appropriate selection of materials and design, it is possible to obtain specific properties in the bimetal. A good example of it is the bimetallic materials, which deflect in proportion to temperature and are used in thermostats and other temperature sensing devices that can be used at high temperatures by appropriately combining high strength and thermal expansion properties (1–3).

If two metals with very different expansion coefficients are bonded together, the obtained assembly will bend in response to temperature. If a bimetal of this type with a length, L, and a total thickness, d, is supported at one end, it can be demonstrated that the curvature will be maximum if:

$$\frac{a_1}{a_2} = \left(\frac{E_2}{E_1}\right)^{1/2} \tag{1}$$

where E_i is the Young's modulus of each material and a_i is its thickness. For many metals $E_1 \approx E_2$ and, in most of the cases, the volume fraction of the two metals is around 50/50. Under these conditions, the following equation can be deduced to express deflection, D, as a function of the change in temperature Δt:

$$D = K\frac{(\Delta t)L^2}{d} \tag{2}$$

and K is a deflection constant including thermal expansion differences and Young's moduli. For a large deflection, K and L have to be maximized and d minimized. Given that the Young's moduli of metals differ slightly, modifications in K have to be carried out through the proper selection of the thermal expansion coefficients. Most bimetallic strips use a very low thermal expansion coefficient material, in most of the cases Invar (Fe–36Ni), bonded (corolled) to a high thermal expansion coefficient material. This last material used to be brass, but now it is either Fe–(∼20)Ni–(∼4)Cr or Mn (∼72)–Cu(∼18)–Ni(∼10) alloys with thermal expansion coefficients above 20 10^{-6} K^{-1}.

The deflection can also be increased by choosing L large and d small. However, in most of the cases, the relation between them is fixed by design given that the bimetallic strip often must exert a force to act on an electric switch or to move a control component, and a compromise is required.

Bimetals are also used to position shadow mask in color TV and monitors.

FABRICATION OF BIMETALS

Although conventional fusion welding techniques are capable of joining certain combinations, it is a slow process and therefore not practical when applied over large areas. Solid-state joining processes (4,5) offer several advantages. A large area can be welded easily and a wide range of dissimilar metals can be joined. Therefore, the fabrication techniques used are based on bonding by diffusion, which involves holding the components under load at elevated temperatures and often imparting important plastic deformation to the assembly formed by the two metals.

This deformation is not always used (6) to produce bimetals, but when it takes place, the codeformation of both materials imposes some flow stress requirements (mechanical compatibility). On the other hand, the diffusion that occurs

during the bonding of both materials at elevated temperature imposes some requirements of mutual reactivity (chemical compatibility). Both aspects are discussed later.

Figure 1 shows some basic manufacturing techniques for producing bimetals with different geometries. The most commercially exploited technique for sheets is roll bonding. In this case sheets of dissimilar metals are cold or hot rolled together to obtain a bimetallic sheet (7,8). This technique is the main one used to produce bimetallic strips for thermostatic elements. In this case, after hot roll bonding, the bimetal is further reduced in thickness by cold rolling and supplied, in most of the cases, as rods or as disks. Hot rolling is also used to produce clad bars (9). In the case of tubes, coextrusion is carried out with a solid tube and a powder or solid outer shell [see Fig. 1(a)]. An alternative route from a solid billet is also being used industrially (10). Hot isostatic pressing (HIP) is a technique widely applied for other types of geometry (11–13).

SOLID-STATE BONDING

Although different methods are used to produce bimetals (4,5), one of the more broadly used techniques is "diffusion bonding" together with its variant "deformation bonding" (6).

Diffusion bonding is a solid-state process by which two surfaces are joined under pressure at an elevated temperature as a result of diffusion-controlled processes. Generally, the surfaces to be bonded are not flat, and the applied pressure must be enough to ensure that the surfaces are in intimate contact. This supposes that a minimum macroscopic deformation is involved in the process. In fact, the amount of deformation distinguishes the so-called "pressure or deformation bonding," where bulk deformation of the parent metals takes place (when bonding and forming are carried out in one operation), from that called "diffusion bonding," where the applied pressures are low, just enough to ensure surface contact. The latter requires a much longer time to complete the process.

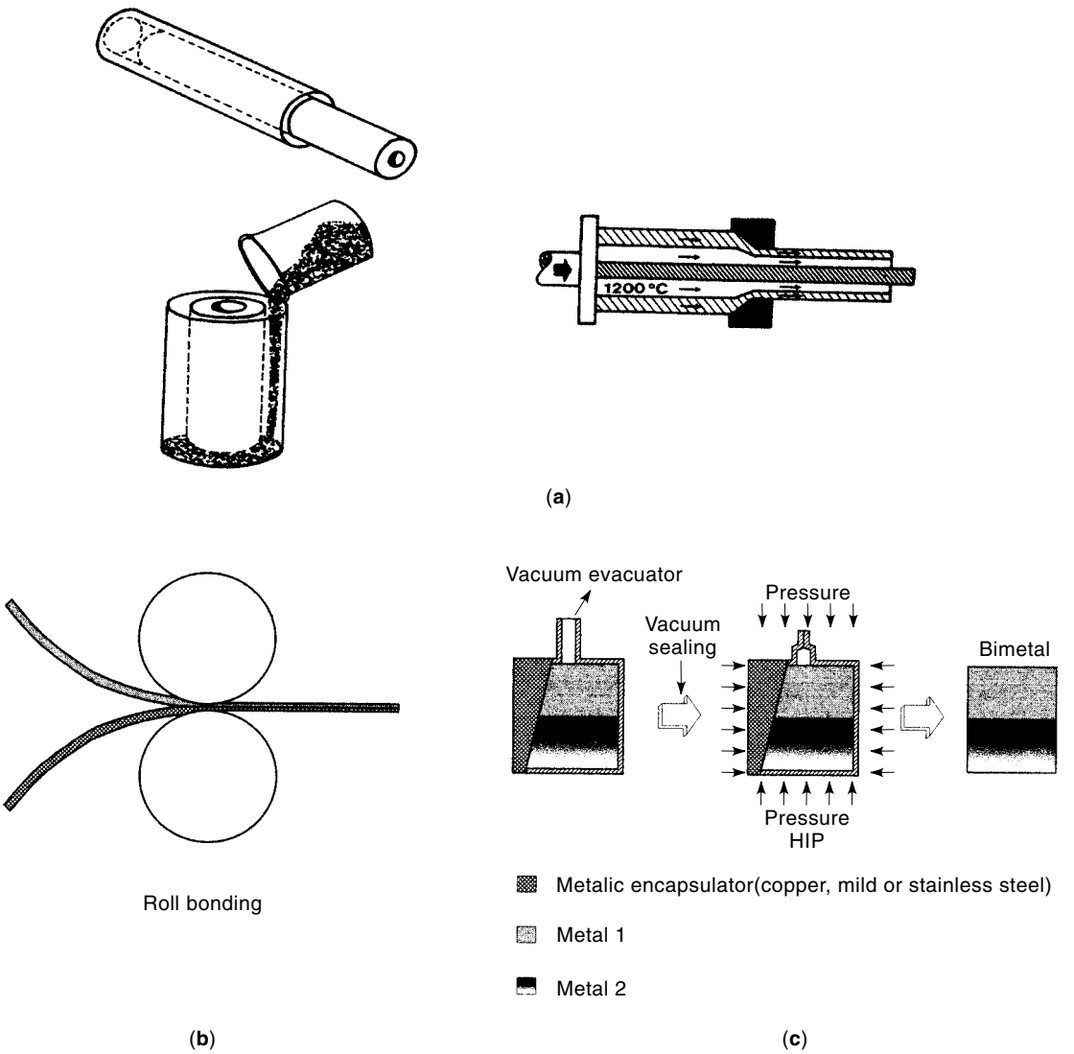

Figure 1. Schematic representation of manufacturing techniques used in the production of bimetals: (a) coextrusion; (b) co-rolling; (c) hipping.

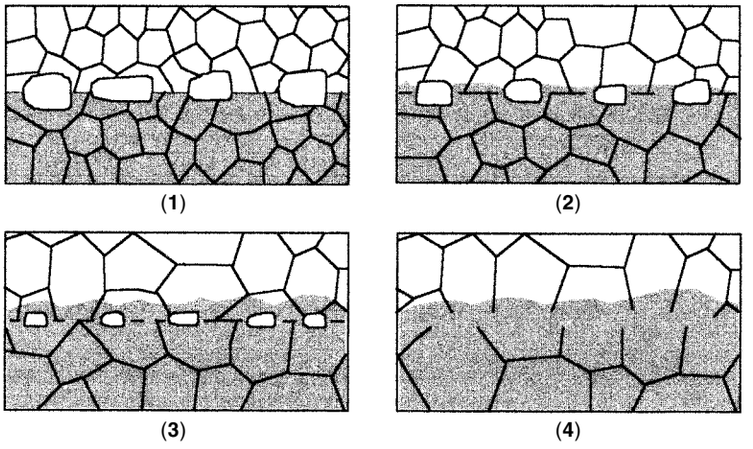

Figure 2. Schematic representation of the different steps in closing porosity during bonding.

This requires using vacuum or inert gas atmospheres to avoid surface deterioration by contamination.

Diffusion bonding in the solid state does not occur by one dominant mechanism, but rather, is a consequence of one or more possible mechanisms that operate singly or in parallel. Each mechanism is assumed to result in material transport so that the energy associated with the interface voids is minimized and its size reduced. The possible mechanisms include (4)

1. Plastic yielding of surface roughness
2. Power-law creep of the surface roughness
3. Surface and volume diffusion that alters the shapes of the voids
4. Grain boundary and volume diffusion from the bond interface to reduce the void volume.

Bonding occurs in two main stages. In the initial stage the plastic deformation of the roughness increases the contact areas until the local stresses decrease below the yield stress. This instantaneous bonding is sometimes called Stage 0, and may result in approximately 10% bonding depending on the process conditions. In a codeformation process, it is the only stage. Then the process continues by shrinkage of irregularly shaped voids that remain between the contacting areas by creep and diffusion mechanisms (Stage I). Finally Stage II begins when the voids become more or less spherical or cylindrical. During this stage the voids shrink and finally disappear by creep and by grain-boundary and volume diffusion from the bond interface. Recrystallization and grain-growth phenomena which occur at these final stages of bonding eliminate the planar grain-boundary interface and increase the strength of the joint. The bonding stages are shown in Fig. 2.

Modeling the diffusion bonding of similar materials has been carried out by several authors (14–24). In these models, rate equations for each of the various material transport mechanisms summarized previously are used in conjunction with material properties and process parameters to predict the extent of bonding under different conditions for different metals. The main differences among the approaches arise from the geometry used for the surfaces, that is, the shapes of the voids and the models used for void shrinkage during diffusion bonding (14). In the earlier approaches (15–17), only one or two mechanisms for diffusion bonding were considered and models were restricted to specific alloys. Derby and Wallach (18,19) developed a void shrinkage model for diffusion bonding including all possible bonding mechanisms. Later on, Hill and Wallach (20), updated this model and included the effect of grain size and the contribution of grain-boundary diffusion to void closure. In these models, it was assumed that all mechanisms occur independently and the total void shrinkage rate can be obtained by a sum of the rate equations for all mechanisms. The predictions of these models have shown reasonable agreement with experimental results for copper and iron. Guo and Ridley (21) developed a new model whose predictions of the bonding time for copper and the Ti-6Al-4V alloy gave better results than the previous models. Furthermore, Pilling and co-workers (22) considered the effect of grain size on diffusion bonding which in addition to the common mechanisms, is of particular significance in superplastic materials (23). One feature common to all of the previous models is that deformation is assumed to occur under conditions of plane strain that reduces the problem to two dimensions. Pilling et al. (24) developed a model for the constitutive equations describing the kinetics of diffusion bonding under an isostatic state of stress. The use of the finite elements methods (FEM) allows modeling the bonding of dissimilar materials and research is being done in this field (25,26). This same method is also being used to model codeformation bonding processes and the conditions under which fracture is produced in extruded tubes (27,28).

The use of interlayers in the form of metallic foils or coatings (electroplated, evaporated, or sputtered), is widespread in diffusion bonding of joints (29). Interlayers lead to reduced values of pressure, time, and temperature used for bonding and involve diffusion welding or diffusion brazing (joining of two metals by producing a liquid at the bond interface) if the melting point of the interlayer is lower than that of the parent metals (30–32). These interlayers must be carefully selected to avoid changes in microstructure or composition (intermetallics formation) which could adversely affect the properties of the bond.

Factors Controlling the Bonding Process

In practice, the properties of the materials to be joined together, such as the diffusion coefficients, their mechanical

properties and the conditions in which the bonding is carried out, define the bond strength. Following are the main process parameters:

- *Pressure.* Required to get contiguity between both materials to be joined on an atomic scale. Pressure causes some local deformation, reduces the roughness of the surface, and increases the contact area between both materials. Creep helps bonding.
- *Deformation.* In principle, the pressure necessary to produce bonding is lower than that required to produce plastic flow of the materials. However, in practice, codeformation is used most times to produce a strong bond. The role of deformation is to break the oxides formed at both surfaces to be bonded, but it can modify the bonding process itself, as can be seen in Fig. 3 (33).
- *Temperature.* Required to increase the bonding rate because it favors creep, plastic deformation, and diffusion. Normally a temperature close to 0.7 T_m is used, where T_m is the melting point of the materials. If bonding is carried out between materials with different melting points, the lower of the melting points is used.
- *Time.* Both creep and diffusion processes are temperature- and time-dependent. Consequently, for a given temperature, a minimum time is required to promote atomic exchange between both materials and closure of the porosity.
- *Surface conditions.* The roughness of the surface defines the contact area of both materials and, consequently, influences the bonding rate. The presence of oxides is very detrimental for diffusion bonding. In certain cases, such as titanium and its alloys, the strong oxide films they form can be removed from the surface by dissolving them in the matrix during the joining operations because of the high solubility of oxygen in these materials (34).

Interface Characterization

Solid-state bonding used to produce bimetals involves atomic interdiffusion across the initial interface to obtain a metallurgical bond. This affects by diffusion a band of material around the interface. This diffusion leads to phase transformation and the formation of new phases, induces grain growth (6), and produces microporosity and the displacement of the interface with respect to external references (Kirkendall effect) (35). Several works show in depth how characterization of the interface is undertaken for different types of bimetals (33,36–40).

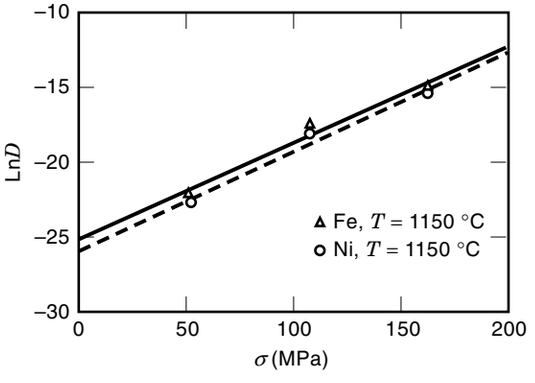

Figure 3. Influence of the applied stress on the diffusion coefficient of Fe and Ni (T = 1150°C) (33).

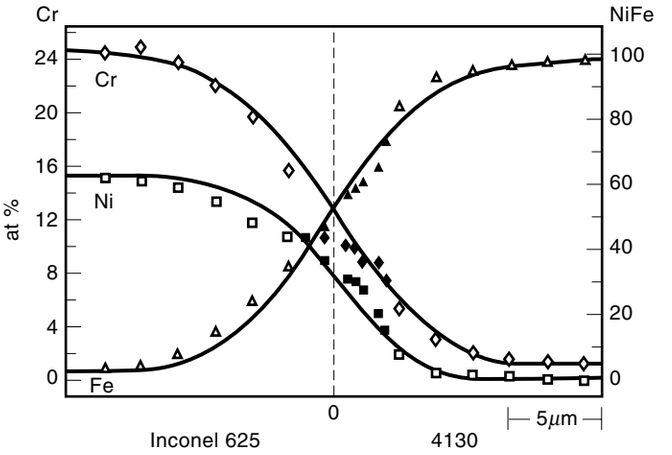

Figure 4. Concentration profiles calculated from Eq. (1) (solid lines) compared to experimental profiles (symbols) for an AISI 4130/Inconel 625 couple bonded by hot pressing at 1050°C (33).

The interdiffusion occurring across the interface produces concentration profiles such as those shown in Fig. 4, for the couple AISI 4130 low allow steel/Inconel 625 (34). Given that the transport of elements is controlled by solid-state diffusion, the extent of solute distribution close to the interface follows error type functions (41,42).

$$C = \frac{C_1 + C_2}{2} - \frac{C_1 - C_2}{2} \operatorname{erf}\left[\frac{x}{2\sqrt{Dt}}\right] \tag{3}$$

where x is the distance from the interface, t is the bonding time, D is the diffusion coefficient, and C_1 and C_2 are the concentrations of the element in both materials, respectively. The curves in Fig. 4 are based on Eq. (3) and the calculated diffusion coefficients of each element (33). Interdiffusion is also analyzed similarly in more complex systems (43,44). Additionally, the possible occurrence of the Kirkendall effect is used to calculate the intrinsic diffusion coefficients (45).

The final strength of the bond is the result of all of the changes in the microstructure. Pores or cavities produced by deficient bonding reduce the toughness and fatigue life. Evaluating bonding requires mechanical tests, some of them specific, and microstructural characterization coupled with fractographic analysis (46). Different mechanical tests are normally used to evaluate the bond strength (47–51). However, certain authors report that the impact test is by far the most sensitive to bond quality, and is directly affected by microporosity (52).

MECHANICAL AND CHEMICAL COMPATIBILITY

As noted previously, pressure and temperature have to be applied and the reaction between the chemical components of the two materials determines how the bond is achieved, its quality, and the nature of the final interface.

Additionally, the industrial process of codeformation is really a deformation process of two dissimilar materials in which bonding also takes place. Therefore, it is clear that the codeformation imposes the conditions, from a mechanical point of view, necessary to carry out the process correctly.

Mechanical Compatibility

The conditions required to bond both materials are related to the relative strength of the materials at the moment of codeformation. The yield stress ratio between the two materials becomes one of the most influential variables (53–55).

In bimetallic tube production, current practice has shown that when the ratio between the strengths of the two materials is below about 2 : 3, the materials are coextruded without problems. When the ratio is higher than these values, some problems occur. Sometimes, for instance, the tube is not smooth and has some protrusions at constant intervals, like bamboo. Therefore, it is important to know the flow stresses of the two materials as a function of the temperature and the strain rate to choose the best conditions for performing the codeformation without problems. Figure 5 shows an example of the mechanical analysis required to find the conditions under which steel AISI 4130 and Inconel 625 are mechanically compatible (56). Note that the compatibility of these materials requires too high a temperature and too low a strain rate and is difficult under industrial codeformation conditions. But this couple is suitable for producing bimetals, if other bonding methods are used (57).

Chemical Compatibility: Case Studies

An equilibrium diagram indicates the different reactions expected during the bonding of two different metals at elevated temperature. In the case of alloys, binary diagrams are not sufficient, and multicomponent diagrams are necessary. Three principal types of binary diagrams occur in welding two pure metals:

1. The two metals form only extended solid solutions. This is very favorable for diffusion bonding, and if the base metals exhibit good strength and ductility, the same properties are found in the region of the bond.
2. The two metals form intermetallic phases and/or limited intermediate extended solid solutions. The effect of such intermetallics on the mechanical properties depends on their size and distribution across the interface. Thin layers strengthen the bond line, whereas thicknesses in excess of 1 μm to 2 μm markedly decrease mechanical properties (58).
3. The two metals are not soluble in the solid state. The bonding operation is much more delicate in this case because adhesion is the main bonding mechanism and is very dependent on the physical and chemical aspects of the interface (59).

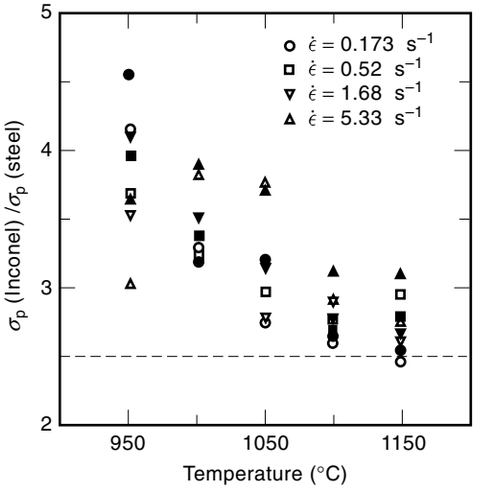

Figure 5. Effect of the strain rate and temperature on the relative strength of Inconel 625 and AISI 4130 low alloy steel (56).

Systems with Extended Solid Solubility. Different bonded carbon steel/stainless steel or Ni, Ni–Fe alloys couples are considered to be in this group. For these combinations, all the substitutional elements have extended solubility at each side of the interface, and no intermetallics are formed. However, the carbon interstitial element of the steel diffuses into the alloy and forms carbides in the matrix or at the grain boundaries.

AISI 4130/2205 Duplex Stainless Steel. The structure obtained at the low alloy steel/duplex stainless steel interface is shown in Fig. 6 (60). A first band (Zone 1) of about 80 μm formed by austenite with $M_{23}C_6$ carbides precipitated at grain boundaries can be seen. As the distance from the interface increases, ferrite begins to replace the carbides at austenite grain boundaries (Zone 2) until the correct austenite/ferrite proportion of the duplex stainless steel is reached (Zone 3).

AISI 4130/INCONEL 625. Figure 7(a) shows a detail of the interface and the region close to it on the Inconel side of the previously mentioned couple obtained by hot extrusion (10,33). The diffusion of carbon from the steel to the superalloy leads to the precipitation of carbides in the latter. Decarburization of the steel close to the interface is denoted by a zone with an increased ferrite percentage compared with the microstructure of the base steel.

Figure 7(b) shows a transmission electron microscope (TEM) image of the region around the bond interface. The Inconel shows a work-hardened substructure of cells and dislocations in addition to carbides rich in Cr, Mo, and Nb. The nature of these carbides is illustrated in Table 1. On the steel side (below the line AA′), a precipitation-free austenite band between 1 and 2 μm wide is formed parallel to the interface by the enrichment of this region of steel with Ni.

AISI 4130-INCOLOY 825. Figure 8(a) shows a detail of the region close to the interface on the Incoloy side of an AISI 4130/Incoloy 825 couple. A large number of carbides rich in Cr and Mo can be observed. In a band of about 10 μm, precipitation takes place both at the grain boundaries and inside the grains, but for greater distances from the interface, carbides are precipitated mainly on the grain boundaries (60).

Figure 8(b) shows a TEM micrograph of the region close to the interface. The line A–A′ represents the interface, which has an undulating appearance at this magnification. The Incoloy shows a work-hardened substructure of cells and dislocations, in which the previously mentioned carbides can be observed. On the steel side (below the line A–A′), some structural arrangement of the bands is apparent. The first band,

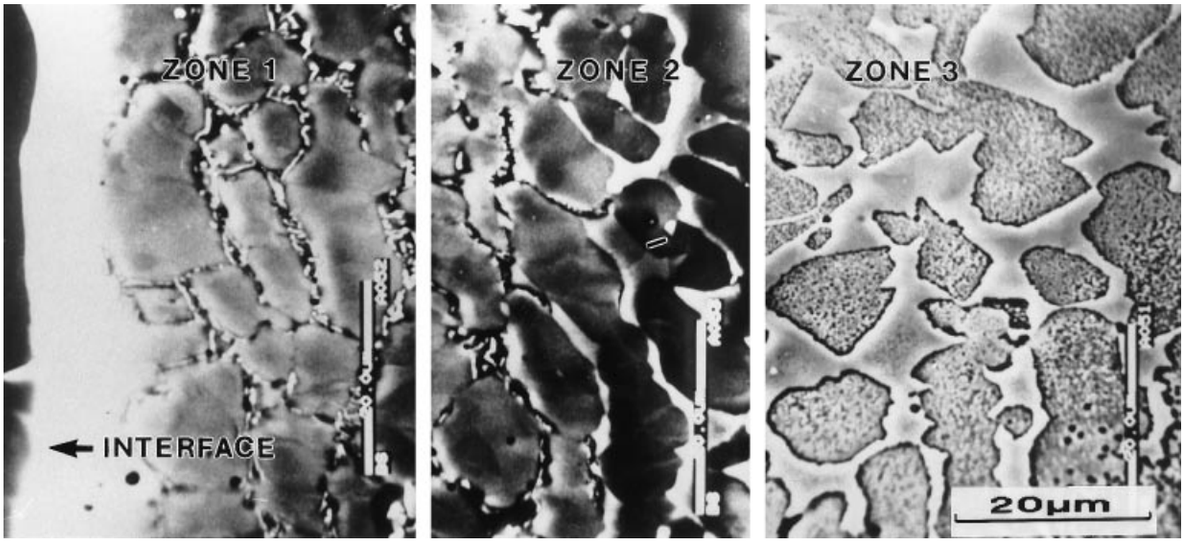

Figure 6. Scanning electron microscope (SEM) image showing the sequence of microstructures at an AISI4130/2205 bonding interface (duplex stainless steel side) produced by hot extrusion (60).

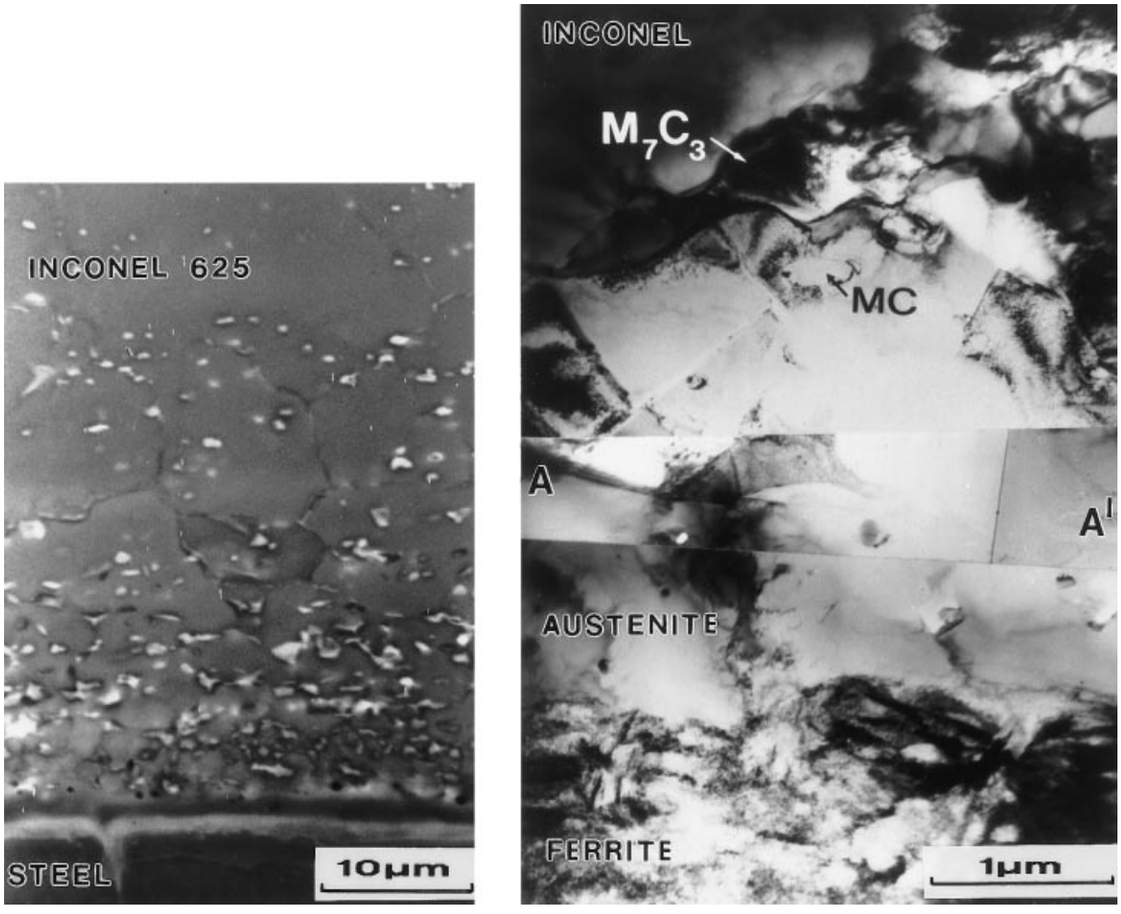

(a) (b)

Figure 7. Region of the interface of an AISI 4130/INCONEL 625 couple bonded by hot extrusion (33): (a) SEM image and (b) TEM image.

Table 1. Types of Carbides Found in the Vicinity of the Interface

Carbides Rich in	Carbide Type, see Ref. 61
Nb	MC
Mo	M_6C
Cr	M_7C_3 (only close to the interface) $M_{23}C_6$

less than 1 μm wide, is formed by austenite grains elongated in a direction parallel to the interface and completely free of precipitates. Twinned plate martensite is formed next to the austenite band. It seems that the concentration of elements diffused from the superalloy in this region is not sufficient to stabilize the austenite but provides adequate hardenability to obtain martensite on cooling. Finally, the steel shows a structure of ferrite and pearlite.

In summary, some common microstructural features can be deduced from the analysis of the different steel/nickel, Ni–Fe or Ni–Cr alloy combinations (62), as illustrated in the scheme representing the evolution of the microstructure around the interface, shown in Fig. 9. To describe clearly the variation of the microstructural features, the region is divided into five zones referred to by Roman numerals.

Zone I: Base Steel. This region corresponds to the base steel. The microstructure is a function of the heat treatment and depends on the cooling rates after bonding (33,60). Close to the interface a higher percentage of ferrite can be observed, denoting decarburization of the steel in this region.

Zone II: Austenite Band. The diffusion of nickel and chromium from the nickel alloy to the steel side at the bonding temperature transforms an increasing volume of the base steel close to the interface to nickel-rich austenite, which remains stable at room temperature. The presence of this band shifts the interface between the austenite and the ferrite toward the steel side.

This austenite band is nearly free of precipitates and probably is caused by its high carbon solubility, agreeing with what has also been suggested by Ayer et al. (38). As a consequence of the more rapid diffusion of chromium and nickel through the grain boundaries, compared with bulk diffusion, this band penetrates along some steel grain boundaries (see Figs. 7 and 8).

Zone III: Large Carbide Precipitation Region. In this region on the nickel alloy side, a copious precipitation of carbides takes place on grain boundaries and inside the grains. These carbides are rich in the carbide-forming alloying elements in the Ni alloy.

Zone IV: Low Precipitation Region. In this region which corresponds to larger distances from the interface, precipitates are found only at the grain boundaries, denoting that carbon also diffuses for longer distances along grain boundaries than in the bulk.

Zone V: Base Nickel Alloy. This region corresponds to the base microstructure of the nickel alloy.

Formation of Intermetallics. A Ti alloy/stainless steel couple is considered here. This combination is a good example of intermetallic forming systems because it is well known that Ti forms a large set of intermetallics with iron, Ni, and Cr (63,64) which are the base of the present steel to be bonded to the titanium alloy. When Ti is bonded to a superalloy, similar behavior is observed (43,65). Other couples of large practical importance also form intermetallics (66–69).

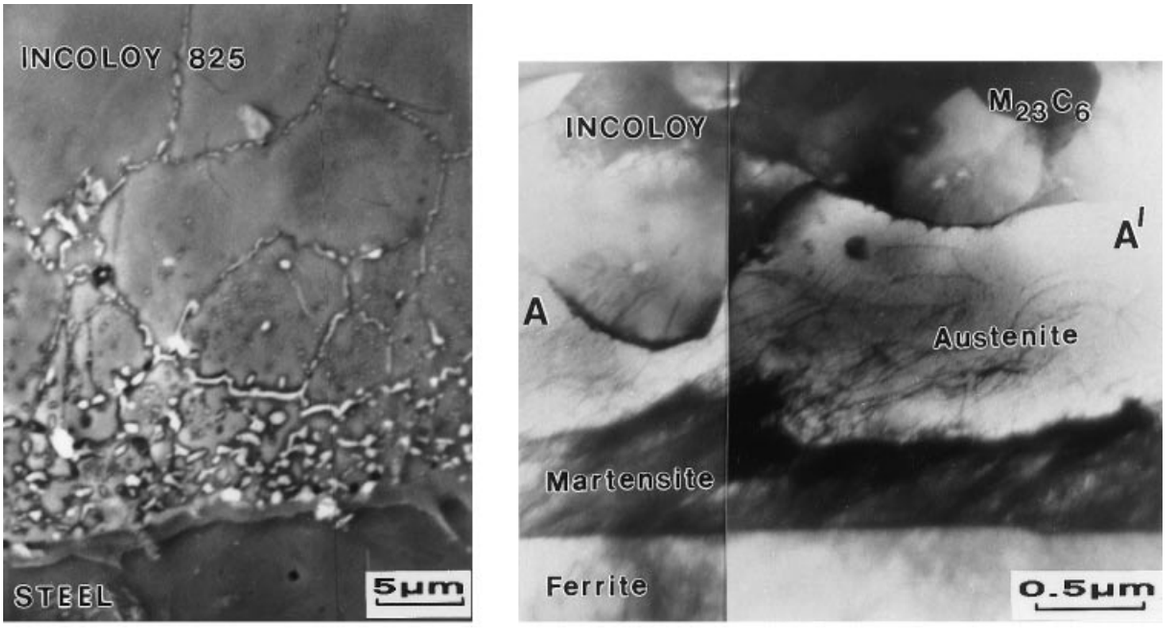

(a) (b)

Figure 8. Region of the interface of an AISI 4130/INCOLOY 825 couple bonded by hot extrusion (60): (a) SEM image and (b) TEM image.

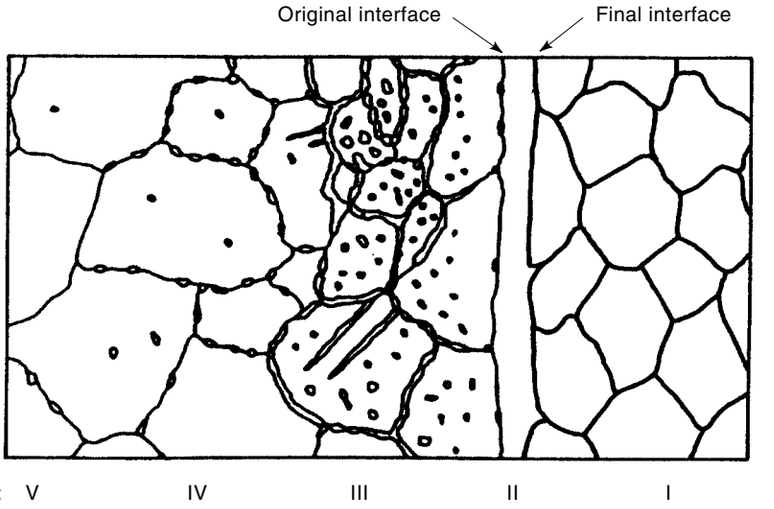

Figure 9. Scheme representing the microstructural evolution close to the steel/nickel alloy interface.

Ti 6242/AISI 316L. Figure 10(a) shows TEM micrographs of a zone close to the interface of the AISI316L-Ti6242 diffusion-bonded couple (44). The A–B lines in the micrograph represent the interface, and some structural arrangement in bands is clearly apparent. The phase sequence across the interface is shown in the corresponding scheme of Fig. 10(b).

Starting from the AISI 316L stainless steel side, a region 1.6 μm wide is formed by the σ phase. Small particles can be observed within this phase, TiC carbide on the grain boundaries and $Ti_5Cr_7Fe_{17}$ χ phase inside the σ grains. Another intermetallic narrow band of an Fe_2Ti phase follows, succeeded by a wider region of about 2 μm formed by a FeTi intermetallic toward the Ti alloy. Within this, some small particles of β-Ti ($<$0.3 μm) appear widely dispersed. There are, also, other kinds of particles, whose chemical composition is compatible with a $\lambda(CrFe)_2Ti$ phase. This $\lambda(CrFe)_2Ti$ phase is located close to the λFe_2Ti phase producing a very narrow (around 0.2 μm) discontinuous band. A narrow region 4, about 0.4 μm wide is also clearly observed, which corresponds to a possible $FeTi_2$ intermetallic phase. However, both crystallographic structures and chemical analyses are also compatible with the Fe_2Ti_4O phase. The oxygen necessary to form this phase probably comes from the initial interface.

Finally, the Ti6242 alloy is observed, and within this alloy at about 0.7 μm from the interface with the last intermetallic, a chain of small particles ($<$0.3 μm) rich in Si and Zr is present. These particles (trapped during the polishing on emery at the free surface of the austenitic 316L stainless steel) indicate the evolution of the original interface showing the occurrence of the Kirkendall effect (45).

The Use of Phase Diagrams. The formation of a complex interface including intermetallic phases in alloys with only partial solubility of their elements makes it difficult to understand the diffusion processes at the bond.

The extension of the different intermetallic and the composition profiles depend on interdiffusion across the different phase interfaces. But the ternary phase diagrams corresponding to the main elements in each couple define, at least qualitatively, the distribution of the different phases. Considering only the major elements Fe, Ti, and Cr in AISI316L-Ti6242 couple, a ternary phase diagram section corresponding to an appropriate temperature can be used (see Fig. 11) (70). If the evolution of the element concentration across the interface is considered, a trajectory, such as that drawn on the previously mentioned phase diagram, is obtained. The region, containing the FeTi intermetallic as a major phase, corresponds to the composition range included between the points A and B in the Fe–Ti–Cr ternary phase diagram. However, a β-Ti phase in equilibrium with the FeTi intermetallic is observed for the higher Ti contents in agreement with observations in Fig. 10, where some particles of this phase are observed into the FeTi band. By lowering the Ti content the composition moves within the region FeTi+β-Ti+λ (a solid solution between Fe_2Ti and Cr_2Ti) of the equilibrium diagram. The presence of several particles, rich in Cr and different from those of free β-Ti (see Fig. 10), experimentally confirms the predictions of the equilibrium diagram. Finally, for the lower Ti content, the composition trajectory is within the region of λ+FeTi of the equilibrium diagram which is compatible with the band in which FeTi and $(Fe,Cr)_2Ti$ phases coexist. The following band of intermetallics found at the interface is that in the composition range between points B and C in the ternary phase diagram of Fig. 11, corresponding to the λ solution formed mainly by Fe_2Ti. The σ phase is not on the diagram at this temperature but can be assumed to form on cooling (44). The particles of the χ phase found experimentally are also predicted by the phase diagram.

The interface formed on the Inconel-Ti6242 couple, analyzed in the previous paragraph, has been described in the same way, using the Ni–Ti–Cr diagram in this case (43).

The Use of Interlayers. Depending on their thickness (58), intermetallics at the diffusion couple interface, produce brittle debonding when tensile stress is applied (71). The assembly fails in tension without any plastic deformation at the interface and at a stress level corresponding to the yield stress of the softer material. If good mechanical properties are required, it is necessary to optimize the bonding operation to avoid the formation of intermetallics (use of interlayers) or to

use very fast bonding systems [explosive bonding (72,73)] to avoid or minimize the formation of brittle intermetallics (74).

One or several thin metallic interlayers aid in ensuring chemical compatibility between the two base materials (75–77). Ultimate tensile strengths above 450 MPa with elongation above 10% have been obtained by diffusion bonding of Zircalloy and austenitic stainless steel, using the sequence of interlayers 304/Cu-V-Ti/Zy (78).

A good material for an interlayer is one presenting extended solid solubility with the other two in between which it is placed, among other properties (79). The phase diagrams allows proper selection. In some cases, no chemical compatibility with both materials to be bonded is possible, and a set of interlayers has to be used. This is the case shown in the micrograph in Fig. 12(a) where the following sequence has been used: AISI 4130/Ni/Cu/V/Ti64. The use of these interlayers avoids forming TiC on the bonding line and the associated very poor quality bonding produced through the inhibition of substitutional element diffusion (44). For steels with low carbon content (stainless steel), in which case Fe and Ti interdiffusion is possible, a similar combination suppresses the formation of intermetallics.

The thickness of the interlayers has to be optimized in terms of the mechanical properties of the assembly and the diffusion distance across the different interfaces during the bonding process. A thick interlayer of a soft material impairs the mechanical response of the assembly. On the other hand, a thin layer allows diffusion across it and the formation of intermetallics [see Fig. 12(b)]. In this case, the σ-Ni_9V_{21} brittle phase has formed by diffusion of Ni over the Cu layer to the next V interlayer during heat treatment after bonding (80).

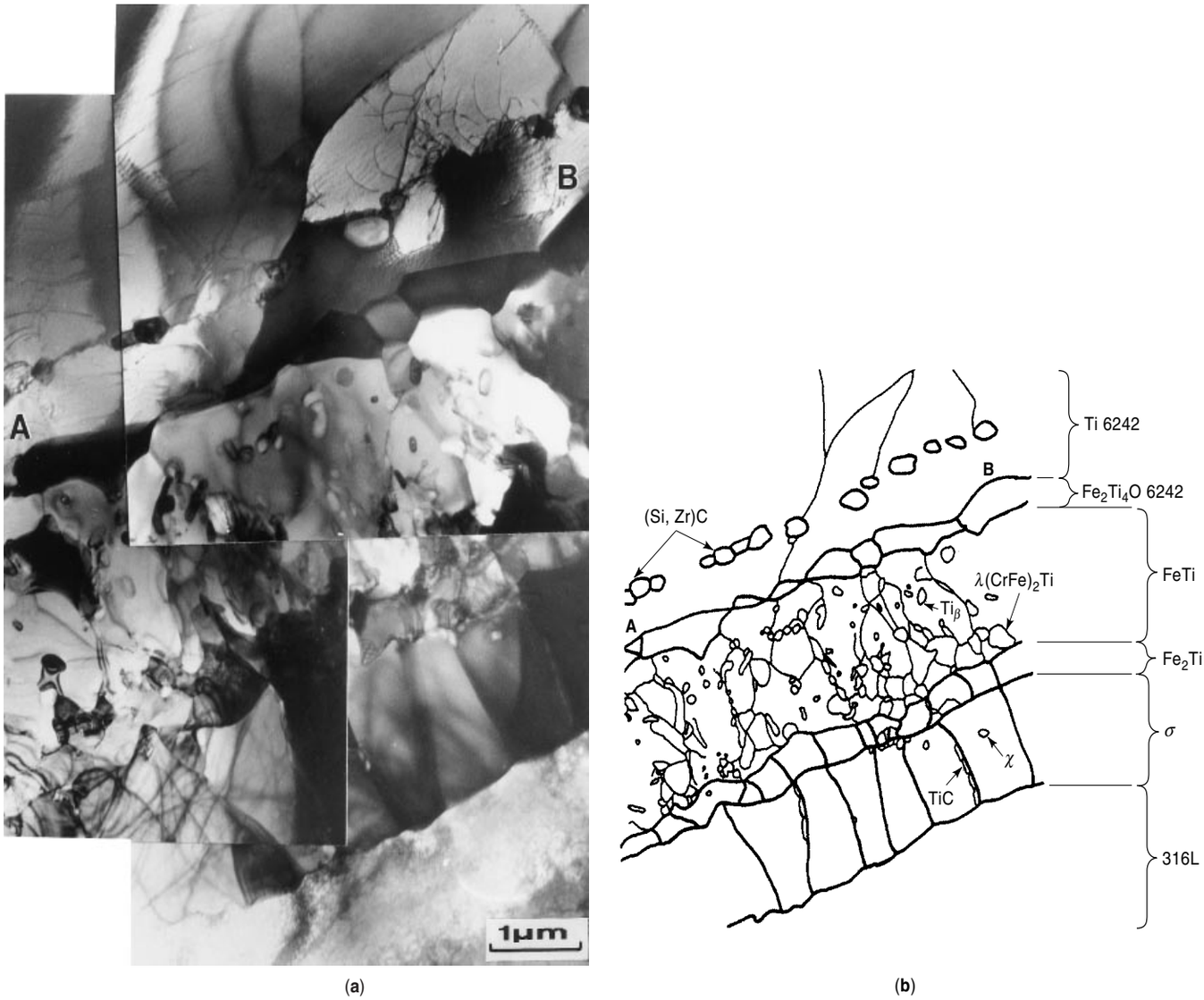

Figure 10. Transmission electron micrograph of the intermetallics at the interface of the couple AISI/316L/Ti6242 diffusion bonded (44).

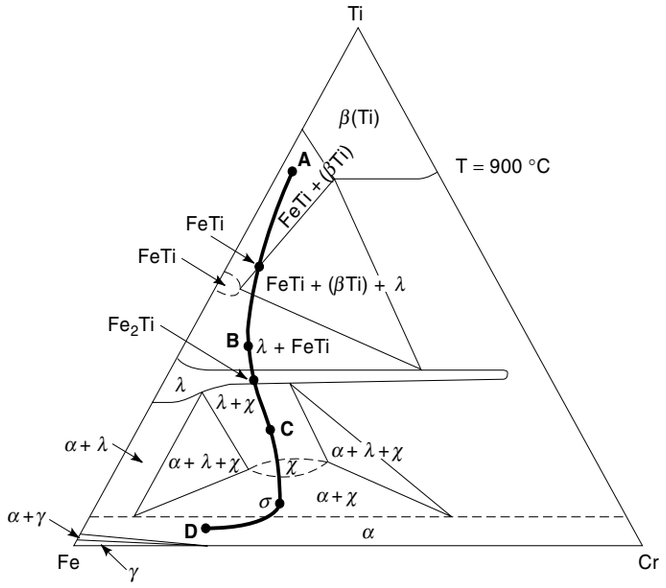

Figure 11. Ternary phase diagram for the Fe–Ti–Cr system (60). The compositional trajectory across the interface after bonding has been drawn as the dark line (44).

Interlayers can be used, as well, with a completely different purpose to modify the properties of the bimetal assembly. In the case of thermostats, the resistivity of both materials forming the bimetal is quite high, and a low resistivity material, like copper or nickel, is used as an interlayer to increase the heating rate (under an imposed voltage).

HEAT TREATMENTS

In certain cases, the thermal cycle given to the materials to join them together by diffusion is not suitable for producing the best combination of properties in each material. Given that the bimetallic material is composed of two different metals or alloys needing different heat treatments, very often the heat treatment for the bimetallic must be a compromise between the treatments appropriate to each of the materials (60,81,82).

Figure 13(a) shows the variation of 0.2% proof stress, ultimate tensile strength, and ductility (measured as elongation to fracture) of a combination AISI 4130/Incoloy 825 with tempering temperature (30 min tempering) following quenching after 30 min of austenitising at 920°C (82). Another example is shown in Fig. 13(b) for the combination AISI 4130/duplex stainless steel with the same conditions of heat treatment as before, except for the austenitising temperature which is now 950°C (81). The hardness of the steel side is also included in both cases. As expected, the mechanical strength and the hardness decrease, and elongation increases with tempering temperature.

Heat treatment involves time and temperature and consequently activates additional diffusion across the interface, as shown in Fig. 14 for carbon (60). Now, the region where chromium carbides are found is broader than that just after bonding (see Fig. 6). The carbide precipitation enhancement produces Cr depletion in the matrix and can be detrimental to the corrosion resistance of the couple. However, in certain cases, with appropriate heat treatment (83), the $M_{23}C_6$ produced in the bonding process in a T11 low alloy steel /347H austenitic stainless steel couple is changed to NbC. In this

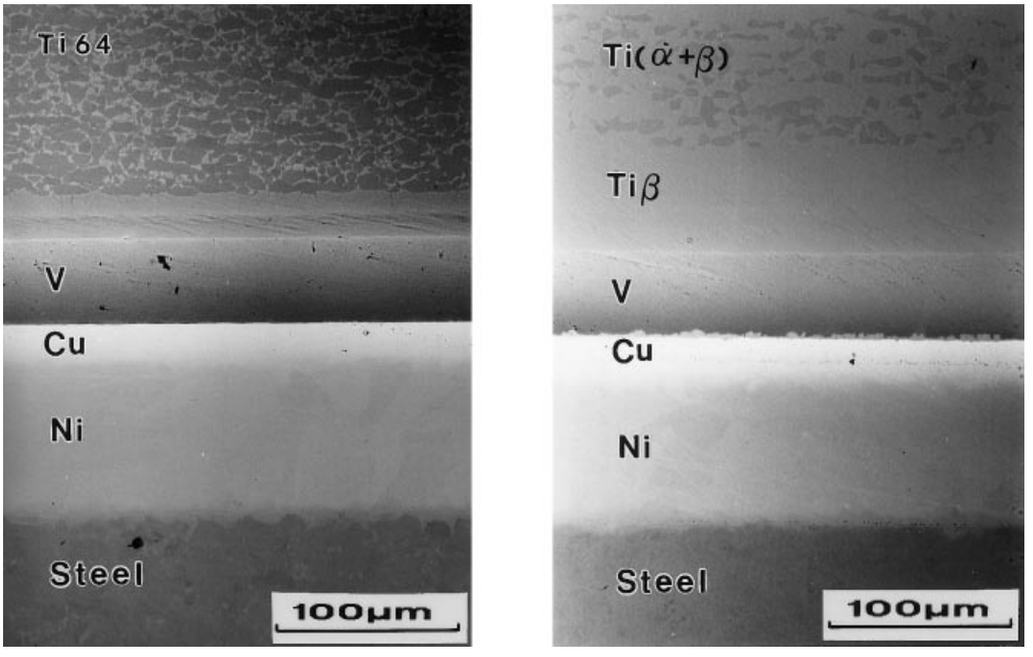

Figure 12. SEM micrographs showing the AISI 4130/Ni/Cu/V/Ti64 interface: (a) after bonding by hot isostatic pressing (HIP) and (b) the same as (a) plus a heat treatment of 15 min at 960°C followed by 60 min at 550°C.

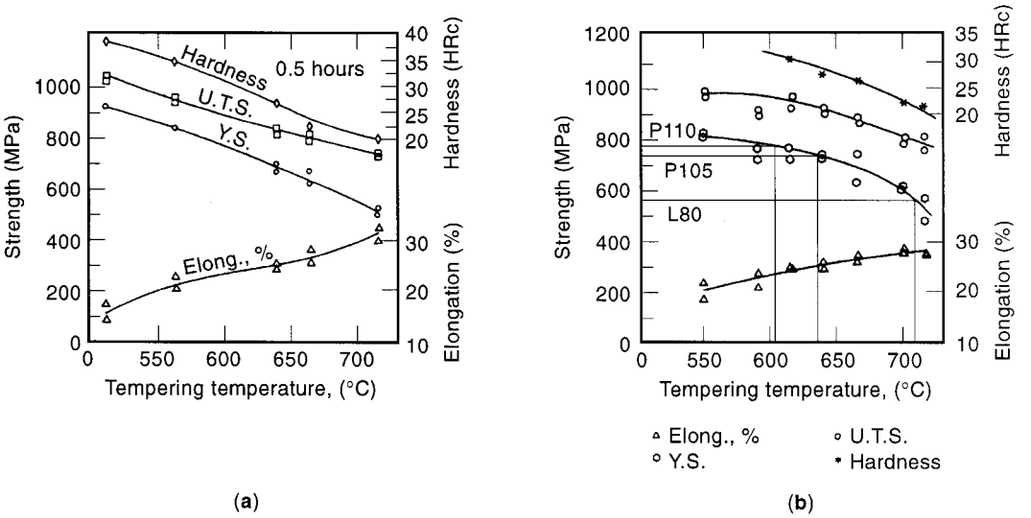

Figure 13. Variation of 0.2% proof stress, ultimate tensile strength, and ductility as a function of the tempering temperature: (a) AISI 4130/Incoloy 825 combination (82) and (b) AISI 4130/ Duplex Stainless Steel (81).

way, the corrosion resistance of the stainless steel cladding is recovered.

MECHANICAL PROPERTIES

When joining dissimilar materials, the mechanical properties of the assembly depend, first of all, on the properties of the base materials and on the quality of the bond. The bonding is of quality if it overcomes a tensile or shear stress corresponding to the flow stress of the softer of the two materials (84–86).

Strength of the Interface

When intermetallics are present at the interface, tensile tests carried out with the tensile axis parallel to the interface produce debonding before the materials finally fracture, as can be seen in Fig. 15 for the Ti/Inconel 625 bimetal (71,80). The effect of such debondings on the flow curve are sudden drops in stress shown in the same figure. Two drops are observed, corresponding to the two bonding interfaces in the three-layer tensile samples analyzed. It can clearly be seen that there is some dispersion in the quality of the interfaces because debonding occurs at different deformations.

Additionally, even when a thick layer of intermetallics is present at the interface, as with the Ti/Inconel 625 couple (43), about a 5% elongation can be applied before debonding proceeds. In this same case and agreeing with the results in Fig. 15, the contribution of bonding $\Delta\sigma_B$ to the strength of the assembly is relatively high (~130 MPa).

The use of interlayers to inhibit the formation of brittle intermetallics during bonding prevents debonding, and a continuous flow curve is obtained, as can be seen in the same figure.

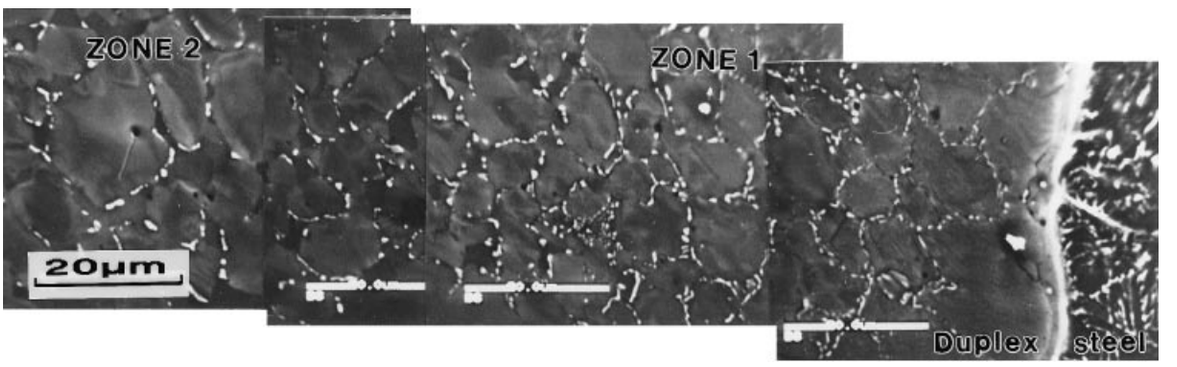

Figure 14. Microstructure at the duplex stainless steel side of the same couple as in Fig. 6, after austenitizing for 30 min at 950°C, quenching, and tempering for 30 min at 550°C (60).

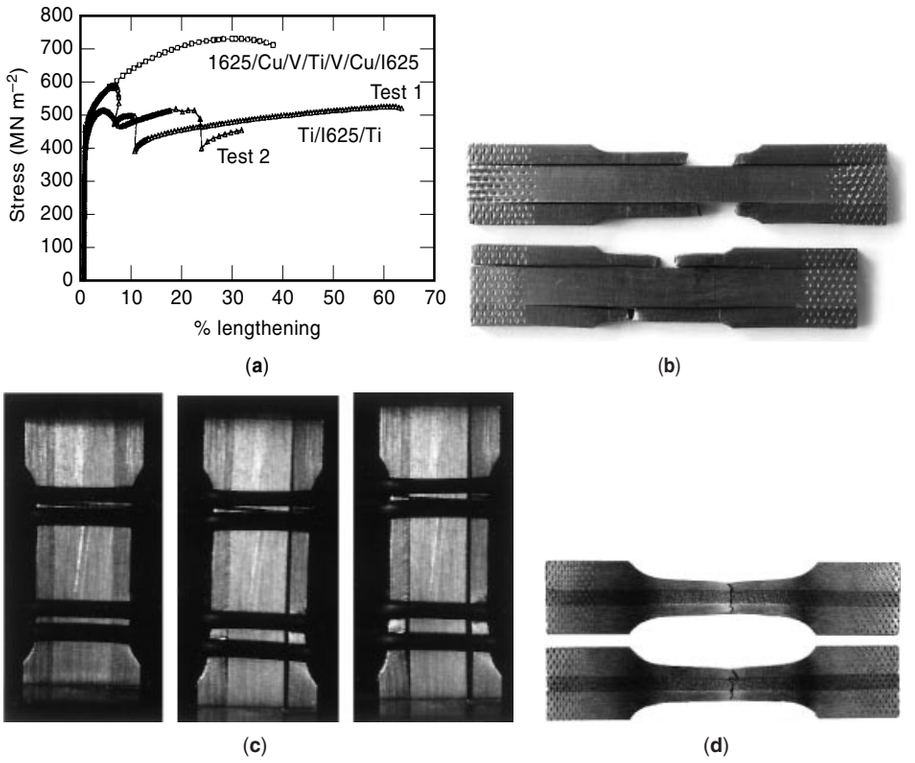

Figure 15. (a) Experimental flow curves for the Ti/Inconel 625/Ti and Inconel 625/Cu/V/Ti/V/Cu/Inconel 625 assemblies. (b) Detail of the debonding at the interfaces. (c) Final fracture of Ti in the first couple. (d) Prevention of debonding in the second assembly when appropriate interlayers are used (71,80).

The Rule of Mixtures

When tested in tension with the tensile axis parallel to the interface, the flow properties of metallic bimetals can be expressed as weighted averages of the component properties and, therefore, can be estimated using constitutive equations of the materials and the rule of mixtures, assuming uniform deformation (87):

$$\sigma_B(\epsilon) = V_1\sigma_1(\epsilon) + (1 - V_1)\sigma_2(\epsilon) \tag{4}$$

where $\sigma_B(\epsilon)$ is the flow stress of the bimetal at strain ϵ, $\sigma_1(\epsilon)$ and $\sigma_2(\epsilon)$ are, respectively, the flow stresses of the two constituents, and V_1 is the volume fraction of the first constituent.

Equation (4) has been used with success for tensile specimens with different volume fractions of bonded materials, as can be seen in Fig. 16 (71,88,89) and has shown generally good agreement with experimental results in continuous fibre-reinforced composites and sandwich sheet materials (50,90,91). However, it has been reported (71) that, for UTS, a best fit to the experimental results is observed when a modified equation is used:

$$(\mathrm{UTS})_B = [V_1\sigma_1(\epsilon_u) + (1 - V_1)\sigma_2(\epsilon_u)]\exp(-\epsilon_u) \tag{5}$$

where ϵ_u is the uniform strain that is calculated from the equation

$$\frac{d\sigma_B}{d\epsilon} = \sigma_B \tag{6}$$

The rule of mixtures is also followed approximately in other bimetallic combinations with and without the use of interlayers (56,71,80).

Application of Finite Elements Method

The tensile behavior of bimetals can also be analyzed by the finite elements method (88,89,92). The results proposed by the FEM analysis for bimetallic specimens indicate the existence of interactions between the two materials during the tensile test under the hypothesis of isodeformation. This interaction produces a modification in the behavior of both materials relative to the behavior of the materials tested individually under the same conditions. The present results indicate that the rule of the mixtures is followed up to the strain at which necking starts. Prediction of these strains for different

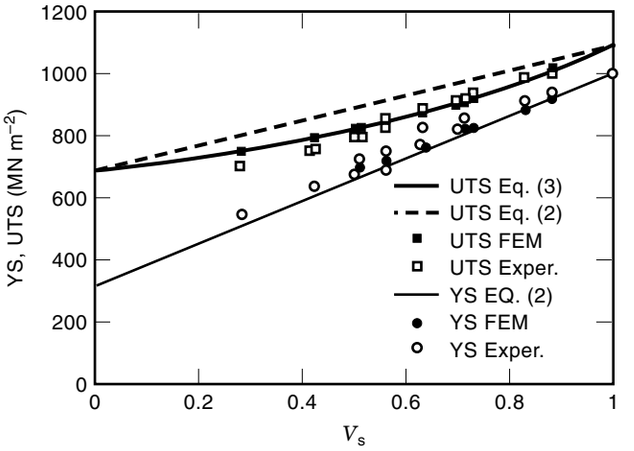

Figure 16. Yield stress and the UTS for the couple AISI 4130/Incoloy 825, as a function of the volume fraction of the steel V_s (71,88,89).

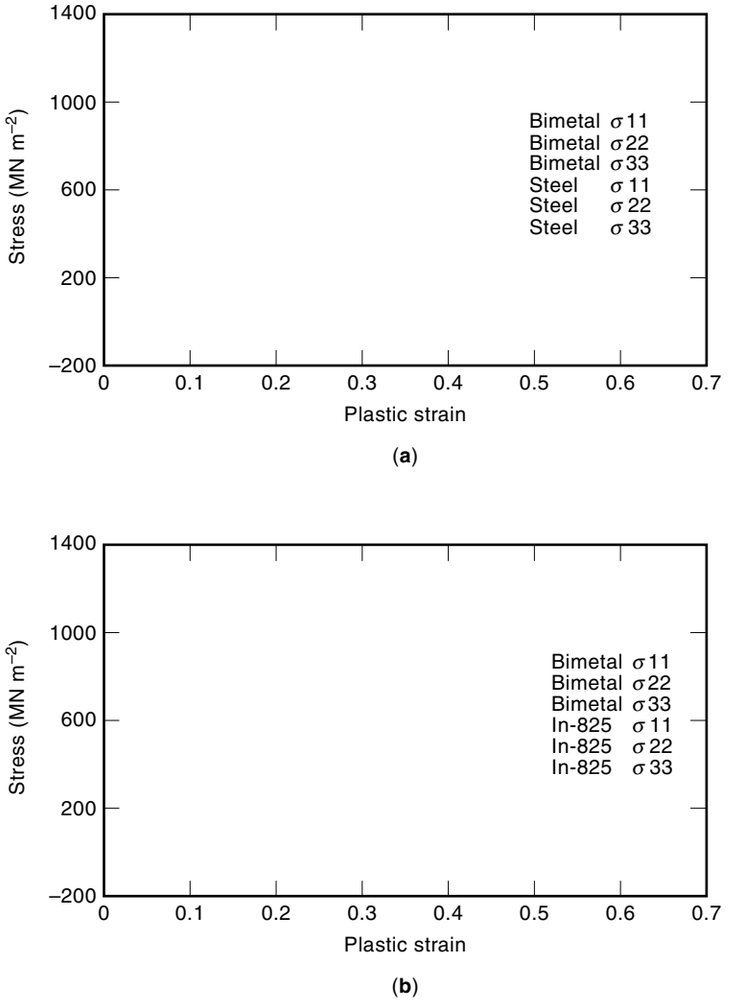

Figure 17. Finite elements method (FEM) stress level developed at: (a) steel, (b) Incoloy, during tensile testing of bimetallic and monolithic specimens. (71,92).

heat treatments and the proportion of the different alloys is crucial for modeling bimetallic behavior. It seems that interaction between the materials produces a complex state of stresses at some point and a premature onset of necking, as has been observed experimentally.

Figure 17 shows the level of the different stresses developed in each material of the previously mentioned 4130 steel and Incoloy 825 couple during tensile tests of bimetallic specimens (71,92). From the figure it is clearly apparent that up to the strain at which necking commences, only the axial stress σ_{11} has a significant value and that the difference in the stresses developed in the same material when it is alone or in the bimetallic specimen is negligible. Once the strain corresponding to necking is reached, the steel in the bimetallic assembly supports lower stresses than when tested individually, and the opposite happens with the Incoloy 825.

In the figures it is also observed that tensile (positive) transverse stresses perpendicular to the interface (σ_{22}) are active and higher for the Incoloy 825 in the bimetallic specimen than when it is tested individually. The opposite happens with the steel.

It has also been shown by the same methods that shear strains participate in the failure of these materials and they must be related to the shear stresses developed. These

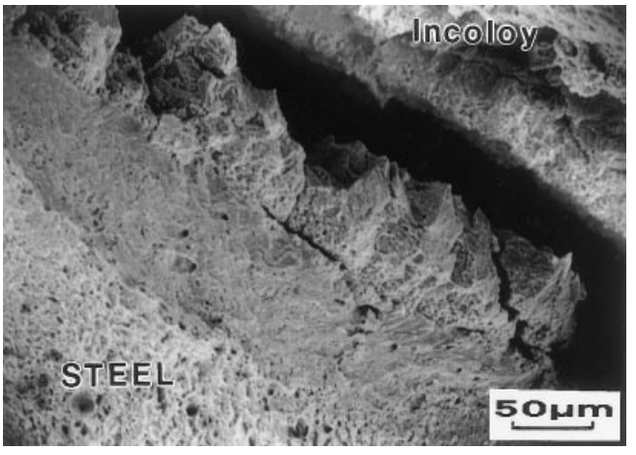

Figure 18. Fracture surface of the AISI 4130/Incoloy 825 couple for which debonding takes place before final fracture (71).

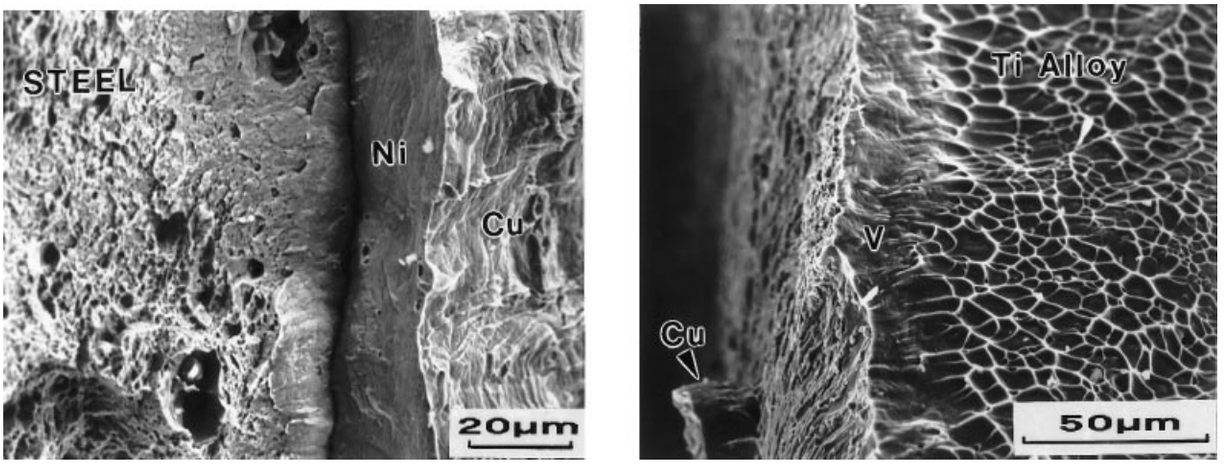

Figure 19. Fracture surfaces of: (a) the AISI 4130 Steel and (b) the Ti alloy, in a region close to the bonding interface where the use of interlayers avoids debonding before final fracture in an AISI 4130/Ti 64 alloy couple (80).

stresses are higher, the higher the proof stress of the steel. These predictions agree with results found experimentally.

FRACTOGRAPHY

Detailed analysis of the fracture of the bimetallic material in tension has shown that a local separation between the two materials occurs before fracture, when a weak region is produced at or close to the interface during bonding because of pores (93), intermetallics (80,94), and carbides (88). The separation between both materials progresses to the weakest region close to the interface, not necessarily to the original interface itself. In a structure similar to that schematized in Fig. 9, it has been observed that debonding progresses inside region III on the Ni alloy side (see Fig. 18) (71,88).

Initially, intergranular shear cracks are generated because of shear stresses (maximum at 45°) in this region weakened by the profuse precipitation of carbides. These originate early during the tensile tests (before necking begins) because of the development of significant shear stresses at 45° ($\tau_{max} \approx \sigma_{11}/2$), given that the other stresses are negligible before necking. The formation of these intergranular shear cracks oriented at 45° has been observed experimentally (71,88). These cracks propagate toward the Incoloy 825 through the region of precipitation, following the grain boundaries (it should be noted that the coarser carbides are precipitated at the grain boundaries). This region is substantially weakened by these cracks (with a smaller effective resisting section) and will fail, even with low stresses perpendicular to the interface, when these develop during necking, as predicted by FEM.

On the contrary, when a pore-free, strong bond is obtained in a system in which no second phases are formed, no debonding is expected to take place before necking, as has been observed with the use of interlayers (see Fig. 19) (80).

ACKNOWLEDGMENTS

The authors wish to express their gratitude to the late Prof. J. J. Urcola for his special leadership over many years in the field of bimetallic materials. Dr. Y. Bienvenu is gratefully acknowledged for his suggestions.

BIBLIOGRAPHY

1. T. D. McGee (ed.), *Principles and Methods of Temperature Measurement,* New York: Wiley-Interscience, 1988, pp. 133–137.
2. W. D. Huston, Temperature Its measurement and control in science and industry, Vol. 3, Part 2 *Applied Methods and Instruments,* London: Chapman & Hall, 1962.
3. S. A. Imphy, *Thermostatic Bimetals,* La Défense, Paris, 1996.
4. E. R. Wallach, *Metallurgist and Materials Technol.,* 71–76, 1984.
5. P. G. Partridge and C. M. Ward-Close, *Metals and Materials,* **1**: 334–339, 1989.
6. Y. Bienvenu et al., in R. Pearce (ed.), *Diffusion Bonding,* Cranfield, England: SIS, 1987, pp. 33–44.
7. N. Bay et al., *Annals of the CIRP,* **34**: 221–224, 1985.
8. E. Romhanji et al., in R. D. Sisson, Jr. (ed.), *Proc. Conf. Coatings Bimetallics Aggressive Environments,* 1985, pp. 53–60.
9. K. Nakasuji, K. Masuda, and C. Hayashi, *ISIJ,* **37**: 899–905, 1997.
10. S. A. Tubacex, European Patent no. 508733 and certificate of addition 517832.
11. G. P. Yiasemides, in R. Pearce (ed.), *Diffusion Bonding,* Cranfield, England: SIS, 1987, pp. 259–267.
12. H. V. Atkinson, M. W. Crabbe, and R. Walker, in D. J. Stephenson (ed.), *Diffusion Bonding 2,* England: Elsevier, 1991, pp. 49–58.
13. H. Zeedijk and R. Van derEerden, *Int. Conf. Hot Isostatic Pressing of Materials,* Antwerp, Belgium, 1988, pp. 3.23–3.28.
14. Y. Takahashi, K. Inoue, and K. Nishiguchi, *Acta Metall. Materialia,* **41**: 3077–3084, 1993.
15. C. L. Cline, *Welding Journal,* 481–489, 1966.
16. C. H. Hamilton, in R. I. Jaffe and M. M. Barte (eds.), *Titanium Science and Technology,* New York: Plenum, 1973, Vol. 1, pp. 625.
17. G. Garmong, N. E. Paton, and A. S. Argon, *Met. Trans.,* **6A**: 1269, 1975.
18. B. Derby and E. R. Wallach, *Metal Science,* **16**: 49, 1982.

19. B. Derby and E. R. Wallach, *Metal Science,* **18**: 427, 1984.
20. A. Hill and E. R. Wallach, *Acta Metall.,* **37** (9): 2425–2437, 1989.
21. Z. X. Guo and N. Ridley, *Materials Science and Technology,* **3**: 945, 1987.
22. J. Pilling et al., *Metal Science,* **18**: 117, 1984.
23. D. A. Miller and T. G. Langdon, *Met. Trans.,* **10A**: 1869–1874, 1979.
24. J. Pilling, *Materials Science and Engineering,* **100**: 137–144, 1988.
25. M. J. M. B. Marques and P. A. F. Martins, *J. Mater. Proc. Technol.,* **26**: 337–348, 1991.
26. Y. Takahashi, T. Koguchi, and K. Nishiguchi, *J. Eng. Mater. Technol.-Trans. ASME,* **115**: 150–155, 1993.
27. J. L. Alcaraz and J. J. Gil-Sevillano, *Proc. "ABAQUS User's" Conf.,* Achen, Germany, 1993, pp. 39–53.
28. J. L. Alcaraz and J. J. Gil Sevillano, *Int. J. Mech. Sci.,* **38**: 157, 1996.
29. M. M. Schwartz, *Metals Joining Manual,* New York: McGraw-Hill, 1979.
30. W. F. Gale and E. R. Wallach, *Metall. Trans. A,* **22A**: 2451–2457, 1991.
31. J. M. Gomez de Salazar et al., *J. de Physique,* **5**: 373–378, 1995.
32. A. A. Shirzadi and E. R. Wallach, *Science Technol. Welding and Joining,* **2**: 89–94, 1997.
33. B. López, I. Gutierrez, and J. J. Urcola, *Mater. Sci. Technol.,* **12**: 45–55, 1996.
34. N. F. Kazakov, *Diffusion Bonding of Materials,* Moscow: Pergamon, 1985, p. 172.
35. D. A. Porter and K. E. Easterling, *Diffusion, Phase Transformations in Metals and Alloys,* London: Chapman & Hall, 1992, pp. 61–109.
36. I. Gutiérrez et al., in D. J. Stephenson (ed.), *Diffusion Bonding 2,* England: Elsevier, 1991, pp. 25–36.
37. B. López, I. Gutiérrez, and J. J. Urcola, in D. J. Stephenson (ed.), *Diffusion Bonding 2,* England: Elsevier, 1991, pp. 37–48.
38. R. Ayer et al., *Metall. Trans.,* **20A**: 665, 1989.
39. D. V. Dunford and P. G. Partridge, *Mater. Sci. Technol.,* **8**: 385–398, 1992.
40. T. Devers, Y. Bienvenu, and R. Porter, Caractérisation mécanique et microstructurale de jonctions acier inoxydable/hafnium réusées par soudage-diffusion-dynanique, *La Revue de Métallurgie-CIT/Science et Génie des Matériaux,* May 1998.
41. Y. Adda and J. Philibert, *La Diffusion dans les Solides,* Tome I and II, Paris: Institute National des Sciences Nucléaires, 1966.
42. J. S. Kirkaldy and D. J. Young, *Diffusion in the Condensed State,* London: The Institute of Metals, 1985.
43. B. Alemán, I. Gutiérrez, and J. J. Urcola, *Metall. Trans. A,* **26A**: 437–446, 1995.
44. B. Alemán, I. Gutiérrez, and J. J. Urcola, *Mater. Sci. Technol.,* **9**: 633–641, 1993.
45. B. Alemán, I. Gutiérrez, and J. J. Urcola, *Scripta Materialia,* **36**: 509–515, 1997.
46. D. V. Dunford and P. G. Partridge, in R. Pearce (ed.), *Diffusion Bonding,* Cranfield, England: SIS, 1987, pp. 17–32.
47. J. Pilling and N. Ridley, *Mater. Science Technol.,* **3**: 353–359, 1987.
48. A. G. Evans et al., *Metal. Trans.,* **21A**: 2419–2429, 1990.
49. J. Harvey, P. G. Partridge, and C. L. Snooke, *J. Mater. Sci.,* **20**, 1009–1014, 1985.
50. S. L. Semiatin and H. R. Piehler, *Metall. Trans.,* **10A**: 85–96, 1979.
51. A. Wisbey and P. G. Partridge, *Mater. Sci. Technol.,* **9**: 441–444, 1993.
52. T. S. Baker and P. G. Partridge, in R. Pearce (ed.), *Diffusion Bonding,* Cranfield, England: SIS, 1987, pp. 73–89.
53. J. L. Alcaraz, J. M. Martínez-Esnaola, and J. Gil-Sevillano, *Int. J. Solid Structures,* **33**: 2075–2093, 1996.
54. J. L. Alcaraz, J. M. Martínez-Esnaola, and J. Gil-Sevillano, *Int. Solids Structures,* **34**, 603–623 and 625–638 (Part II), 1997.
55. J. L. Alcaraz, J. Gil-Sevillano, and J. M. Martínez-Esnaola, *J. Mater. Proc. Technol.,* **61**: 265–274, 1996.
56. B. López, Ph.D. Thesis, Facultad de Ciencias, University de Navarra, San Sebastián, Spain, 1993.
57. B. López, I. Gutierrez, and J. J. Urcola, *Materials Characterisation,* **28**: 49–59, 1992.
58. A. Fuji, K. Ameyama, and T. H. North, *J. Mater. Sci.,* **31**: 819–827, 1996.
59. M. Hourcade, *Soudage et Techniques Connexes,* May–June 1989, pp. 48–56.
60. I. Gutierrez et al., *Mater. Sci. Technol.,* **7**: 761–769, 1991.
61. J. Steeds, (The Bristol Group), *Convergent Beam Electron Diffraction of Alloy Phases,* Bristol: A. Hilger, 1984.
62. B. López et al., in M. Fuentes et al. (eds.), *Key Engineering Materials,* Switzerland: Trans Tech, 1997, Vols. 127–131, pp. 695–702.
63. M. Hansen, *Constitution of Binary Alloys,* New York: McGraw-Hill, 1958.
64. S. Hinotani and Y. Ohmori, *Trans. Jpn. Inst. Metals,* **29**, 116–124, 1988.
65. B. Alemán, I. Gutiérrez, and J. J. Urcola, in M. Fuentes et al. (eds.), *Key Engineering Materials,* Switzerland: Trans Tech, 1997, Vol. 127–131, pp. 703–710.
66. F. A. Calvo et al., *J. Mater. Sci.,* **23**: 2273–2280, 1988.
67. I. Kawakatsu and S. Kitayame, *Trans. Jpn. Inst. Metals,* **18**, 455–465, 1977.
68. W. C. Johnson and R. W. Heckel, *Metall. Trans. A,* **12A**: 1693–1697, 1981.
69. L. S. Castleman and L. L. Seigle, *Trans. Metall. Soc. AIME,* 589–596, 1958.
70. V. Raghavan, in *Phase Diagrams of Ternary Iron Alloys,* London: The Institute of Metals, 1987, p. 43.
71. T. Guraya, B. Aleman, and J. J. Urcola, in M. Fuentes et al. (eds.), *Key Engineering Materials,* Switzerland: Tarns Tech, 1997, Vols. 127–131, pp. 869–876.
72. C. T. Wang and R. Hardwick, Industrial Applications of Ti and Zr: Fourth Volume, ASTM STP 917, C. S. Young and J. C. Durham (eds.), Philadelphia: American Society for Testing and Materials, 1986, pp. 85–98.
73. P. Lefrancois et al., *Mem. et Etudes Scientifiques de la Rev. de Metallurgie,* **89**, 27–37, 1992.
74. S. B. Dunkerton, *Welding Inst. Res. Bull.,* **23**, 388–395, 1982.
75. A. Wisbey, C. M. Ward-Close, and I. C. Wallis, *Mater. Sci. Eng.,* **A208**: 93–100, 1996.
76. R. Lison, *Le Soudage dans le Monde,* **23** (5/6): 125–129, 1985.
77. K. Bhanumurthy et al., *J Nuclear Mater.,* **217**, 67–74, 1994.
78. M. Huet, M. Hourcade, and B. Hocheid, *Mem. et Etudes Scientifiques Rev. de Metallurgie,* **6**: 313–325, 1988.
79. J. L. Jellison and F. J. Zanner, *Metals Handbook,* 9th ed., Metals Park, Ohio: American Society for Metals, 1983, Vol. 6, pp. 684–691.
80. B. Aleman, Ph.D. Thesis, Facultad de Ciencias, University de Navarra, San Sebastián, Spain, 1996.
81. J. Saucedo, T. Guraya, and J. J. Urcola, *Prakt. Metallogr.,* **30**: 452–468, 1993.
82. J. Saucedo, Master Thesis, ESII, University de Navarra, San Sebastián, Spain, 1990.

83. J. A. Berroeta et al., *Proc. Conf. Advanced Heat Resistant Steels for Power Generation,* San Sebastian, Spain, 1988.
84. T. Devers and M. Hourcade, in D. J. Stephenson (ed.), *Diffusion Bonding 2,* England: Elsevier, 1991, pp. 171–182.
85. R. A. Ricks et al., in D. J. Stephenson (ed.), *Diffusion Bonding 2,* England: Elsevier, 1991, pp. 69–82.
86. F. A. Calvo et al., in D. J. Stephenson (ed.), *Diffusion Bonding 2,* England: Elsevier, 1991, pp. 144–157.
87. G. E. Arkulis, *Compound Plastic Deformation of Layers of Different Metals,* Jerusalem: Daniel Davey, 1965.
88. T. Guraya, Ph.D. Thesis, Facultad de Ciencias, University de Navarra, San Sebastián, Spain, 1994.
89. J. J. Urcola, *Design with Advanced Materials and Composites,* April 27–29, 1994, Dept. Continuing Education, Oxford University, UK.
90. J. G. Beese and G. M. Bram, *J. Eng. Mater. Technol.,* **97**: 10–13, 1975.
91. D. N. Lee and Y. K. Kim, *J. Mater. Sci.,* **23**: 1436–1442, 1988.
92. T. Guraya, J. R. Ocina, and J. J. Urcola, *Mater. Sci. Technol.,* **11**, 595–599, 1995.
93. I. D. Kedrin and A. G. Fesenko, *Autom. Weld.,* **31**: 20–23, 1978.
94. G. K. Kharchenko, V. M. Falchenko, and V. F. Maznko, *Autom. Weld.,* **27**: 15–18, 1974.

I. GUTIÉRREZ
B. LÓPEZ
B. ALEMÁN
CEIT and University of Navarra

BINARY COUNTERS. See COUNTING CIRCUITS.

BINARY PHASE SHIFT KEYING. See PHASE SHIFT KEYING.